Effective vertical diffusion by atmospheric gravity waves

Han-Li Liu[1,1]

[1]National Center for Atmospheric Research, P. O. Box, 3000, Boulder, CO 80307-3000

November 30, 2022

Abstract

Quantification of heat and constituent transport by gravity waves in global models is challenging due to limited model resolutions. Current parameterization schemes suffer from over-simplification and often underestimate the transport rate. In this study, a new approach is explored to quantify the effective vertical eddy diffusion by using a high-resolution WACCM simulation based on scale invariance. The WACCM simulation can partially resolve the mesoscale gravity wave spectrum down to ~250 km horizontal wavelength, and the heat flux and the effective vertical eddy diffusion by these waves are calculated directly. The effective vertical diffusion by the smaller-scale, unresolved waves, is then deduced based on scale invariance, following the method outlined by Liu (2019) in quantifying gravity wave momentum flux and forcing. The effective vertical diffusion obtained is generally larger than that obtained from parameterizations, and is comparable with that derived from observations in the mesosphere and lower thermosphere region.

Effective vertical diffusion by atmospheric gravity waves

Han-Li Liu[1]

[1]High Altitude Observatory, National Center for Atmospheric Research, Boulder, Colorado, USA

Key Points:

- Vertical heat flux follows scale invariance with a shallow spectrum.
- Effective vertical diffusion by resolved and unresolved waves are calculated using scale invariance.
- The diffusion coefficient is comparable with values obtained from observations.

Corresponding author: H.-L. Liu, `liuh@ucar.edu`

Abstract

Quantification of heat and constituent transport by gravity waves in global models is challenging due to limited model resolutions. Current parameterization schemes suffer from over-simplification and often underestimate the transport rate. In this study, a new approach is explored to quantify the effective vertical eddy diffusion by using a high-resolution WACCM simulation based on scale invariance. The WACCM simulation can partially resolve the mesoscale gravity wave spectrum down to 250 km horizontal wavelength, and the heat flux and the effective vertical eddy diffusion by these waves are calculated directly. The effective vertical diffusion by the smaller-scale, unresolved waves, is then deduced based on scale invariance, following the method outlined by Liu (2019) in quantifying gravity wave momentum flux and forcing. The effective vertical diffusion obtained is generally larger than that obtained from parameterizations, and is comparable with that derived from observations in the mesosphere and lower thermosphere region.

Plain Language Summary

Atmospheric gravity waves may transport heat and chemical species in the vertical direction. Such transport, often measured in terms of an effective diffusion over the large-scale background atmosphere, can be important in controlling the exchange of energy and mass between the lower and upper atmosphere, but quantification of the transport process is challenging because gravity waves are not well resolved or not resolved at all in global models. Previous formulation to approximate the transport tends to over-simplify the process, and can lead to model biases. In high resolution models, the larger scale part of the gravity waves are resolved and the transport by these waves can be directly calculated from simulation results. This study shows that the transport flux of heat follows scale invariance–a statistical similarity over scales–within the resolved mesoscale range. This scale invariance is used to derive the transport flux by the unresolved waves. It is shown that the transport by the unresolved waves can contribute significantly to the total wave transport. The effective diffusion coefficient derived from this study is comparable to values obtained from observations.

1 Introduction

Gravity waves (GWs) play a critical role in transporting momentum, heat and constituents throughout the atmosphere. Their effects need to be parameterized in general circulation models (GCMs), because GWs are a sub-grid scale process (Alexander et al., 2010). This was demonstrated as being essential to model the zonal wind reversal and the anomalous winter-to-summer temperature gradient in the mesosphere/mesopause region by Holton (1982, 1983), who used the linear saturation theory (Lindzen, 1981) to parameterize the drag by breaking GWs. It is also shown in later studies that GW drag is important for driving the stratospheric quasi-biennial oscillation (QBO) (Baldwin et al., 2001) and the mesospheric semi-annual oscillation (MSAO) (Dunkerton, 1982; Sassi & Garcia, 1997).

GW dissipation is found to induce a net heat flux, which has been determined from a linear theory (Walterscheid, 1981). This is in addition to the diffusion by turbulence induced by GW breaking as formulated in Lindzen (1981). The same idea applies to the transport of constituents, and the wave induced heat/constituent flux has been formulated in terms of an effective eddy diffusion coefficient (Garcia et al., 2007; A. Z. Liu, 2009; Gardner & Liu, 2010). The formulation by Garcia et al. (2007) is applied in the Whole Atmosphere Community Climate Model (WACCM). Although diffusion from gravity wave breaking is found to play a secondary role in tracer transport in comparison to advection (Holton & Schoeberl, 1988), WACCM simulations by Garcia et al. (2014) demonstrated that the CO_2 distribution above ∼80 km depends sensitively on the effective eddy diffusion coefficient. Furthermore, the values from WACCM (∼5 to 50 m^2s^{-1} between

80–100 km) are found to be smaller than those determined from observations (Swenson et al., 2019), and those required for achieving agreement with various measurements of constituents (Feng et al., 2013; Garcia et al., 2014; Randall et al., 2015; Orsolini et al., 2017; Smith-Johnsen et al., 2018).

Beyond monochromatic wave consideration, Walterscheid and Hocking (1991) suggested that the superposition of a random set of GWs may result in significant parcel dispersion and vertical diffusion in the mesosphere and lower thermosphere (MLT), based on a quasi-linear theory and parcel trajectory simulations. The same study also suggests that the eddy diffusion coefficient obtained from wave flux calculation can oscillate between large down-gradient (positive) and counter-gradient (negative) values.

The combined effects of superposition of transient, finite amplitude, and dissipating GWs associated with a myriad of wave sources are not tractable analytically and thus not easily parameterized. Modeling study by GCMs, on the other hand, also faces its own challenges. The foremost challenge is the forbidding cost of simulating the full range of mesoscale GWs, including the wave sources, wave propagation, and wave dissipation in the whole atmosphere environment. It is, however, possible for whole atmosphere models to partially resolve the GW spectrum with the current computing power down to several hundred km (e.g., H.-L. Liu et al. (2014); Becker and Vadas (2018)). Effective eddy diffusion coefficient has been calculated for the resolved waves (Grygalashvyly et al., 2012). Large effective diffusion has also been suggested based on scaling argument using high-resolution WACCM results (H.-L. Liu, 2017). The challenge for such modeling study is how to maintain the physical consistency between the resolved and parameterized GW effects (the gray zone challenge, (Vosper et al., 2016; H.-L. Liu, 2019)). A strategy to address this challenge is to deduce the effect by unresolved waves from the resolved wave effect based on scale invariance (H.-L. Liu, 2019). This method has been used to calculate the vertical flux of the GW horizontal momentum and the associated zonal forcing (H.-L. Liu, 2019). In this study, this method is applied to the calculation of vertical eddy diffusion by GWs.

2 Numerical Model

A high-resolution version of WACCM is used in this study. Detailed description of the model and simulations is found in H.-L. Liu et al. (2014) (and references therein). A brief summary is provided here. WACCM is one of the atmosphere components of the NCAR Community Earth System Model (CESM), with the vertical domain extending to 5.9×10^{-6} hPa ($\sim$145 km). The spectral element (SE) dynamical core is used in this study. It is based on a cubed-sphere, with a quasi-uniform horizontal resolution of $\sim$25 km and a 0.1 scale height vertical resolution above 40hPa (and higher below). A July simulation with parameterized wave drag (H.-L. Liu, 2017, 2019) is used for the current study. The gravity wave parameterization scheme used in the standard WACCM configuration (Richter et al., 2010) has been adjusted (H.-L. Liu, 2017) to obtain realistic mean wind and temperature structures.

3 Analysis

We first examine the zonal wavenumber power spectra of potential temperature θ and vertical wind w and their co-spectrum–the spectrum of vertical heat flux. From Figure 1(a), it is seen that the power spectrum of θ ($P_\theta(k)$, k is the zonal wavenumber) follows a power-law distribution between zonal wavenumber 10 and 100, with a slope of -1.9. This is similar to the power spectrum of potential temperature found in the troposphere (Nastrom & Gage, 1985). The power spectrum of the vertical wind ($P_w(k)$) follows a power-law with a much shallower slope (-0.7), as noted in previous studies (Bacmeister et al., 1996; Lane & Knievel, 2005; Lane & Moncrieff, 2008; H.-L. Liu, 2019). As in the case of the vertical momentum flux (H.-L. Liu, 2019), the shallow slope of the vertical wind leads to a shallow spectrum of vertical heat flux. As seen in Figure 1(c): the vertical heat flux spectrum ($S_{w\theta}(k)$) has a slope of -1.3, which is the average value of the slopes of $P_\theta(k)$ and $P_w(k)$. Similar spectral features are found at other altitudes and latitudes, and Figures 1 (d-f) show the latitudinal dependence of spectral slopes of $P_\theta(k)$, $P_w(k)$, and $S_{w\theta}(k)$ at stratospheric, mesospheric and lower thermospheric altitudes (30, 75, and 90 km, respectively), with the slope calculated using a method described in H.-L. Liu (2019). The latitudinal and height dependence of the spectral slope of $S_{w\theta}(k)$ are very similar to those of the vertical momentum flux (Figure 1 of H.-L. Liu (2019)): the spectral slope variability is larger at lower altitudes, and the largest deviation from the nominal "mean" value (downslope of 7/6) is found at southern (winter) stratosphere and lower mesosphere (below ∼70 km), likely resulting from the "run-away" jet therein due to missing gravity wave forcing.

It is noted that the full spectrum of heat flux $S_{w\theta}(k)$ has both upward (positive) and downward (negative) values, corresponding to counter-gradient and down-gradient fluxes, respectively, with respect to zonal mean potential temperature ($\overline{\theta}$). Overall the down-gradient flux is larger than the counter-gradient flux, as expected, and the spectral components of the counter-gradient fluxes may result from flow transience, nonlinearity, and its spectral transform. In Figure 1(c-f), only the down-gradient components and their slopes are plotted.

An effective vertical eddy diffusion coefficient, in the zonal mean sense, can be calculated from the heat flux and the vertical gradient of zonal mean potential temperature

$$K_{zz} = -\overline{w'\theta'}/(\partial\overline{\theta}/\partial z) \tag{1}$$

with primes denoting perturbation around zonal mean. Here we will focus on the contribution from gravity waves, and the flux term can be calculated from spectral integration between the cutoff zonal wavenumbers on the low and high ends, $k^<$ and $k^>$, respectively:

$$K_{zz}^{<>} = -\int_{k^<}^{k^>} S_{w\theta}(k)dk/(\partial\overline{\theta}/\partial z) \tag{1$'$}$$

$k^<$ is set to 10 here, and $k^>$ should be set to 1000–2000 to cover the full mesoscale range. However, the model can only resolve wavenumber up to $k^|$ due to limited model resolution. With a quasi-uniform resolution of ∼25 km, the current model can effectively resolve waves with horizontal wavelength of 200 to 250 km. The $k^|$ is set to zonal wavenumbers corresponding to wavelength 250 km at each latitude. Part of the total effective eddy diffusion coefficient $K_{zz}^{<>}$ can be directly calculated from the resolved waves, which is denoted as $K_{zz}^{<|}$, using Equation 1$'$ but between wavenumber $k^<$ and $k^|$. On the other hand, the effective eddy diffusion coefficient from higher wavenumbers, $K_{zz}^{|>}$, cannot be properly accounted for because these waves are unresolved or under-resolved. However, it can be deduced from $K_{zz}^{<|}$ by using scale invariance, like the vertical flux of zonal momentum and zonal forcing (H.-L. Liu, 2019):

$$K_{zz}^{|>}/K_{zz}^{<|} = \begin{cases} ((k_>/k_|)^{1-\alpha} - 1)/(1 - (k_</k_|)^{1-\alpha}) & \text{if } \alpha \neq 1 \\ \ln(k_>/k_|)/\ln(k_|/k_<) & \text{if } \alpha = 1 \end{cases} \tag{2}$$

where α is the down-slope value of the spectrum. As noted above, there are wave components with upward heat flux, and the apparent K_{zz} associated with these spectral components would be negative ($K_{zz}(k^-) < 0$). Both the positive and negative spectral values, $K_{zz}(k^+)$ and $|K_{zz}(k^-)|$, display power-law distribution, though their slopes could be different. The spectral calculation described above is performed separately for the two, and then summed (with sign) to obtain the net K_{zz}.

Figures 2(a-c) show the K_{zz} by the resolved waves ($K_{zz}^{<|}$), by the under-/un-resolved waves deduced from Equation 2 ($K_{zz}^{|>}$), and the sum of the two. The parameterized K_{zz}

is shown in (d) for comparison. $K_{zz}^{<|}$ increases with altitude, from 10^{-3}–10^{-2} m^{2}s^{-1} in the lower stratosphere to $\sim 10^2$ m^{2}s^{-1} in the lower thermosphere. Its latitude-height structure is similar to that of the zonal forcing by gravity waves (H.-L. Liu, 2019). $K_{zz}^{|>}$ also has a similar spatial structure, and its magnitude is comparable to or even larger than $K_{zz}^{<|}$. $K_{zz}^{|>}$ is over 1000 m^{2}s^{-1} at high latitudes in the southern stratosphere and lower mesosphere. This is due to the over-flattening of the wave spectra therein, as can be seen from Figure 1(d). For example, the spectral slope is 0 around 50°S at 30 km, and according to Equation 2 $K_{zz}^{|>}$ would be $\sim$10 times larger than $K_{zz}^{<|}$. This over-flattening of the wave spectra is caused by the unrealistically large winter jet, which is in turn due to insufficient gravity wave forcing (H.-L. Liu, 2019).

The total $K_{zz}^{<>}$ ($K_{zz}^{<|} + K_{zz}^{|>}$) has similar spatial structure and magnitude to the parameterized K_{zz}^{P} in the mesosphere (70-85 km) (though at SH higher latitudes the former is generally larger). At altitudes below and above $K_{zz}^{<>}$ is larger than K_{zz}^{P}. This is because the parameterization used is based on the linear saturation theory for wave breaking (Lindzen, 1981), and in WACCM it has been tuned so that much of the wave breaking occurs around MLT to reverse the zonal wind. It is worth noting that the latitude/height structure of $K_{zz}^{<>}$ is in good agreement with that of the absolute momentum flux derived from satellite observations from the stratosphere to the lower thermosphere (Ern et al., 2018). $K_{zz}^{<>}$ is thus more realistic than K_{zz}^{P}.

Averages globally, over the northern/southern hemispheres (NH/SH) poleward of 30° and over the tropical region of $K_{zz}^{<|}$, $K_{zz}^{|>}$, $K_{zz}^{<>}$, and K_{zz}^{P} are shown in Figure 3(a). The equivalent transport coefficient K_{adv} associated with the residual-mean vertical velocity, $\overline{w}^r$, is calculated as

$$K_{adv} = |\widehat{\overline{w}^r\overline{\theta}} / \frac{\partial\overline{\theta}}{\partial z}| \tag{3}$$

following Holton and Schoeberl (1988), and its area-weighted averages (hat sign) are shown in respective plots. It is noted that an alternative method is to define K_{adv} as $|\overline{w}^r \frac{\partial\overline{\theta}}{\partial z} / \frac{\partial^2\overline{\theta}}{\partial z^2}|$, since this would apparently facilitate direct comparison of the advective term and the diffusive term. However, $\frac{\partial^2\overline{\theta}}{\partial z^2}$ is close to 0 at some latitudes and altitudes, making it difficult to interpret the result. On the other hand, at altitudes where this second order derivative is finite, the transport coefficients calculated from the two methods are found to be comparable. The mean molecular diffusion is also plotted for comparison. By comparing the global mean of $K_{zz}^{<|}$ and $K_{zz}^{|>}$, it is seen that the two are comparable between $\sim$70–95 km, and the latter (diffusion by unresolved waves) is larger/smaller at lower/higher altitudes. As discussed earlier, $K_{zz}^{|>}$ becomes extremely large in the southern stratosphere and lower mesosphere at higher latitudes, where the wave spectra become excessively flat. This is also reflected in the global average. The total K_{zz} and K_{zz}^{P} are comparable at 75 to 80 km. At lower altitudes, K_{zz}^{P} is 2–3 orders of magnitude less than the total K_{zz}, and is actually similar to the molecular diffusion between 20 and 50 km. K_{zz}^{P} also decreases rather quickly with altitude above 75 km, and crosses the molecular diffusion coefficient profile at 90 km. The homopause height according to K_{zz}^{P} is thus 15–20 km too low compared with the accepted value (105–110 km) (Schunk & Nagy, 2009; Andrews et al., 1987). On the other hand, the total K_{zz} increases with altitude above 70 km, and becomes equal to the molecular diffusion coefficient profile at 103 km. In comparison with K_{adv}, the total K_{zz} is less at all altitudes below 100 km, except when it becomes unrealistically large near $\sim$50 km. This is consistent with the conclusion reached by Holton and Schoeberl (1988), that the vertical eddy diffusion is in general secondary to advective transport. However, hemispheric and latitudinal dependence are noted in the comparison (Figure 3(b-d)): K_{zz} and K_{adv} become more comparable in the winter hemisphere (SH) in the mesosphere and lower thermosphere (especially at higher latitudes). The NH and SH difference in K_{adv} results from the different temperature structure: The temperature increases with altitude at a faster rate–thus has a shorter vertical scale–in the winter MLT than in the summer, due to the adiabatic heating associated with the downwelling driven by gravity wave drive. This result suggests that the vertical diffusion can play an important role in the vertical transport in winter time MLT at higher latitudes.

It is found that the total K_{zz} calculated using the method outlined here does not have a sensitive dependence on $k^{|}$. The K_{zz} shown in the figures is obtained by setting $k^{|}$ to zonal wavenumbers corresponding to 250 km zonal wavelength for each latitude. The calculation has been repeated by changing the horizontal wavenumber to 400 km (with the small and large wavenumber cutoffs unchanged), and the total K_{zz} obtained is similar.

4 Discussion

The effective diffusion may result from gravity wave dissipation (Walterscheid, 1981) and dispersion by randomly superposed gravity waves (Walterscheid & Hocking, 1991; Lukovich & Shepherd, 2005). Nonlinearity can also lead to apparent transport, but it may not act coherently on the mean flow over time, and considerable cancelation may occur when averaged over time (Walterscheid & Hocking, 1991; Nakamura, 2001). As such, the diffusion coefficient deduced from wave flux calculation (Equation 1) (i) may vary significantly over time, and (ii) is not positive definite. This issue is examined here. As discussed in the previous section, down-gradient and counter-gradient fluxes are separated when analyzing the heat flux spectrum, and so are the calculations of the diffusion coefficients by the resolved and unresolved waves. In Figure 4, the positive and negative $K_{zz}^{<|}$ and $K_{zz}^{|>}$ and their sums are shown at several altitudes. The values in the NH and the SH are shown separately, since the $K_{zz}^{|>}$ values in the two hemispheres can differ significantly. It is seen from the figure that at all the altitudes and latitudes the total $K_{zz}^{<|}$ and $K_{zz}^{|>}$ are positive, indicating the flux calculation using potential temperature can indeed yield the net down-gradient flux. It is also seen that the values of the positive and negative K_{zz} (equivalently the down and counter gradient heat fluxes) are several times larger than the net values. This confirms the findings by Walterscheid and Hocking (1991) that there is considerable cancelation between the two.

Figure 4 also shows that the latitudinal dependence of $K_{zz}^{<|}$ and $K_{zz}^{|>}$ can be different. For example, at 90 km $K_{zz}^{<|}$ has similar values at the equator and at middle northern latitudes (net values between 10–20 m^2s^{-1}), but $K_{zz}^{|>}$ values at middle northern latitudes is much larger than the equatorial values (over 30 m^2s^{-1} vs nearly 0). This is because of the latitudinal dependence of the spectral slope. As seen from Figure 1(f), at 90 km the slope is much flatter at middle northern latitudes (down slope value $\sim$0.8) than at the equator (down slope value $\sim$1.4). The spectral slopes of the positive and negative K_{zz} (down and counter gradient fluxes) can also be different, with the former generally flatter than the latter (thus the positive net $K_{zz}^{|>}$ values).

The average eddy diffusion coefficient obtained here (Figure 3) is comparable to that deduced from observations in the MLT region. For example, the total K_{zz} shown in Figure 3(a) between 90–95 km is 30–50 m^2s^{-1}. Salinas et al. (2016) derived eddy diffusion from SABER CO_2 measurement, and it is $\sim$33 m^2s^{-1} at 90 km. Swenson et al. (2019) obtained global mean eddy diffusion coefficient from O determined by SABER OH measurements, with odd oxygen loss considered, and the value is 33–60 m^2s^{-1} between 90–95 km. This is smaller than the eddy diffusion coefficient from an earlier estimate without considering the odd oxygen loss (Swenson et al., 2018). It is also smaller than the mean eddy diffusion coefficient estimated from O determined from SCIAMACHY measurements (70–90 m^2s^{-1} for the same altitude range). It is worth noting that at 97 km, the total K_{zz} from Figure 3(a) is $\sim$60 m^2s^{-1}. This is less than the eddy diffusion coefficient applied at the lower boundary of TIE-GCM ($\sim$97 km) by Qian et al. (2009), 200–250 m^2s^{-1} around June solstice, to obtain agreement of the thermospheric density between TIE-GCM simulation and that inferred from satellite drag. However, the effective diffusion coefficient obtained in that study is a measure of all dynamical effects not included in the model, including large-scale processes such as mean circulation and tidal effects (Jones Jr. et al., 2017). For example, K_{adv} is between 100 and 200 m^2s^{-1} according to Figure 3(a).

As mentioned in the Introduction, previous numerical experiments suggested that the vertical eddy transport in WACCM tends to be too weak. For example, Feng et al. (2013) found from a 1-D model that an effective diffusion coefficient of $\sim$200 m^2s^{-1} is needed for 80–90 km at mid-latitude to sustain a meteoric input of more than 20 td^{-1}, while the parameterized K_{zz} from that WACCM version used was 5 m^2s^{-1} and could only sustain a meteoric input of 2.1 td^{-1}. The total K_{zz} from the calculation presented in this study is $\sim$45/30 m^2s^{-1} at 90km and 40°N/S. This is still less than the required value of $\sim$200 m^2s^{-1}. However, eddy diffusion is the only transport process considered in the 1-D model, and large-scale dynamics would account for a significant portion of the vertical transport. For example, the transport coefficient corresponding to the downward residual circulation in the winter hemisphere is between 45-80 m^2s^{-1} within the 80–90 km altitude range (Figure 3(c)). Other studies also found the need to increase the parameterized K_{zz} by decreasing the effective Prandtl number (Garcia et al., 2014; Orsolini et al., 2017; Smith-Johnsen et al., 2018). For example, a much better agreement between simulated and observed CO_2 in the MLT can be achieved when the Prandtl number is reduced by half, thus doubling the global mean K_{zz} from 7, 20, and 45 m^2s^{-1} to 14, 40 and 90 m^2s^{-1} at 80, 90 and 100 km, respectively (Garcia et al., 2014). The latter set of values are comparable to the NH averaged values shown in Figure 3.

Vertical effective diffusivity (Nakamura, 2001) by gravity waves in the MLT has been computed from numerical experiments using an off-line coupled model of the dynamics and chemistry (Kuehlungsborn Mechanistic general Circulation Model–MEsospheric Chemistry-Transport Model, or KMCM-MECTM), both by full dynamical fields from the simulation and by dynamical fields with the resolved smaller scales (350–1000km) filtered out (Grygalashvyly et al., 2012). The effective diffusion coefficients obtained, which are by waves with the horizontal scales between 350–1000 km, have spatial structures similar to the total K_{zz} in Figure 2, with an upward-poleward tilting mesosphere peak between 60–90 km in the NH, a "mixing barrier" layer of $\sim$5 km above, and further increases above that. The spatial structure in the winter hemisphere is also similar, except for the very large values found in the stratosphere and lower mesosphere "cold pole" in the current study. The MLT values from that study, however, are much larger than those obtained here, with mesospheric maximum values in the summer hemisphere over 350 m^2s^{-1} at 60° latitude between 80–85 km, and maximum in the winter hemisphere at 100 km reaching 500 m^2s^{-1} at middle to high latitudes. They are also larger than the values determined from observational and parameterization studies mentioned above. The larger values would also imply a higher turbopause. The cause of this discrepancy is unclear and needs to be determined in future studies, when atmosphere constituents are included in high-resolution WACCM simulations.

5 Summary and Conclusion

The zonal wavenumber spectrum of the vertical heat flux calculated from a high-resolution WACCM simulation is shown to follow a power-law distribution in the resolved mesoscale range. The spectral slope varies with latitude and height, and is similar to the slope of the vertical flux of horizontal momentum flux (H.-L. Liu, 2019). They are shallower than the spectral slopes of zonal spectra of kinetic and potential energies, likely due to the flat vertical wind spectrum. The smaller scale waves can thus contribute significantly to the total vertical fluxes.

The vertical eddy diffusion coefficient (K_{zz}) is calculated from the ratio between the vertical heat flux and the vertical gradient of zonal mean potential temperature. The contribution from the resolved gravity waves to K_{zz} (and equivalently the vertical heat flux), can be directly calculated from the co-spectra of potential temperature and vertical wind. The contribution by under-resolved and unresolved waves can be deduced from the resolved portion of the spectra based on scale invariance, following the method discussed in H.-L. Liu (2019). The calculation is performed separately for the down-gradient heat flux (positive K_{zz}) and for the counter-gradient flux (negative K_{zz}). The two have large cancellations, and the net heat flux is down-gradient and the total K_{zz} is positive. Eddy diffusion coefficients by smaller scale, unresolved waves are indeed comparable or even larger than that by resolved waves.

The K_{zz} values are in general agreement with vertical eddy diffusion values deduced from observational and parametric studies. The globally averaged total K_{zz} increases consistently with altitude, and is equal to molecular diffusion at $\sim$103 km, consistent with the homopause altitude. This study thus provides a method to directly calculate the effective vertical diffusion by gravity waves when the waves are partially resolved by the model. The total K_{zz} thus obtained are generally larger than that from gravity wave parameterization, except in the mesosphere where the two become comparable. This is probably because the gravity wave parameterization scheme in the model has been tuned to reproduce the wind and temperature structures in the mesosphere/mesopause region. The parameterized K_{zz} is thus likely underestimating the vertical transport in the lower thermosphere, a region critical for controlling atmosphere-geospace mass exchange, as well as the vertical transport below the mesosphere.

Figure 1. Zonal wavenumber power spectrum density (PSD) of (a) potential temperature and (b) vertical wind at the equator and 75 km altitude. (c): the zonal wavenumber spectrum of the vertical heat flux at the same location. The thin straight lines in the plots indicate the power-law slope, and the slope values are marked by the lines. Downslope values of the heat flux spectrum (solid line) and PSD of potential energy (dotted line) and vertical wind (dashed line) at (d) 30 km, (e) 75 km and (f) 90 km. These are averages over 7 days (3–9 July).

Figure 2. Effective diffusion coefficient by (a) resolved waves, (b) unresolved waves and (c) the sum of the two. (d): monthly mean parameterized eddy diffusion coefficient for July according to Garcia et al. (2007).

Figure 3. Averages (a) globally, over (b) NH and (d) SH poleward of 30°, and (c) the tropical region of the effective eddy diffusion coefficient by resolved waves (blue dotted line), unresolved waves (blue dashed line), and their sum (blue solid line). In comparison, the black solid line is the molecular diffusion, the red solid line is the parameterized eddy diffusion coefficient, and the black dash-dot line is the equivalent transport coefficient by residual-mean vertical velocity (Equation 3).

Figure 4. The down-gradient (dotted line) and counter-gradient (dashed line) eddy diffusion coefficients and their sum (solid line) by the resolved waves (red) and unresolved waves (navy blue) at (a, b) 30 km, (c, d) 75 km, and (e, f) 90 km, and for the NH (a, c, e) and the SH (b, d, f).

Acknowledgments

I thank Noboru Nakamura and Daniel Marsh for valuable discussions. This effort is partially supported by NASA Grants 80NSSC20K1323, 80NSSC20K0601, 80NSSC20K0633, 80NSSC17K0007, and NSF Grant OPP 1443726. National Center for Atmospheric Research is a major facility sponsored by the National Science Foundation under Cooperative Agreement No. 1852977. Numerical simulations were performed on NWSC/NCAR Yellowstone and Cheyenne Supercomputers with computing resources provided by the NCAR Strategic Capability (NSC) allocation and the Computational and Information Systems Laboratory (CISL) at NCAR. NCAR CESM/WACCM is an open-source community model, and is available at https://doi.org/10.5065/D67H1H0V. Model output used for this study is available at https://doi.org/10.5065/rxae-ab06.

References

Alexander, M. J., Geller, M., McLandress, C., Polavarapu, S., Preusse, P., Sassi, F., … S.Watanabei (2010). Recent developments in gravity-wave effects in climate models and the global distribution of gravity-wave momentum flux from observations and models. *Quart. J. Roy. Meteor. Soc.*, *136*, 1103-1124.

Andrews, D. G., Holton, J. R., & Leovy, C. B. (1987). *Middle atmosphere dynamics.* Orlando, Florida: Academic Press.

Bacmeister, J. T., Eckermann, S. D., Newman, P. A., Lait, L., Chan, K. R., Loewenstein, M., … Gary, B. L. (1996). Stratospheric horizontal wavenumber spectra of winds, potential temperature, and atmospheric tracers observed by high-altitude aircraft. *Journal of Geophysical Research: Atmospheres*, *101*, 9441–9470. doi: 10.1029/95JD03835

Baldwin, M. P., Gray, L. J., Dunkerton, T. J., Hamilton, K., Haynes, P. H., Randel, W. J., … Takahashi, M. (2001). The quasi-biennial oscillation. *Reviews of Geophysics*, *39*, 179-229. doi: 10.1029/1999RG000073

Becker, E., & Vadas, S. E. (2018). Secondary gravity waves in the winter mesosphere: Results from a high-resolution global circulation model. *Journal of Geophysical Research: Atmospheres*, *123*, 2605?2627. doi: 10.1002/2017JD027460

Dunkerton, T. J. (1982). Theory of the mesopause semiannual oscillation. *Journal of the Atmospheric Sciences*, *39*, 2681-2690.

Ern, M., Trinh, Q. T., Preusse, P., Gille, J. C., Mlynczak, M. G., Russell III, J. M., & Riese, M. (2018). Gracile: a comprehensive climatology of atmospheric gravity wave parameters based on satellite limb soundings. *Earth System Science Data*, *10*, 857–892. doi: 10.5194/essd-10-857-2018

Feng, W., Marsh, D. R., Chipperfield, M. P., Janches, D., Höffner, J., Yi, F., & Plane, J. M. C. (2013). A global atmospheric model of meteoric iron. *Journal of Geophysical Research: Atmospheres*, *118*, 9456-9474. doi: 10.1002/jgrd.50708

Garcia, R. R., López-Puertas, M., Funke, B., Marsh, D. R., Kinnison, D. E., Smith, A. K., & González-Galindo, F. (2014). On the distribution of CO2 and CO in the mesosphere and lower thermosphere. *Journal of Geophysical Research: Atmospheres*, *119*, 5700–5718. doi: 10.1002/2013JD021208

Garcia, R. R., Marsh, D. R., Kinnison, D. E., Boville, B. A., & Sassi, F. (2007). Simulation of secular trends in the middle atmosphere, 1950-2003. *J. Geophys. Res.*, *112*. doi: 10.1029/2006JD007485

Gardner, C. S., & Liu, A. Z. (2010). Wave-induced transport of atmospheric constituents and its effect on the mesospheric na layer. *Journal of Geophysical Research: Atmospheres*, *115*. doi: 10.1029/2010JD014140

Grygalashvyly, M., Becker, E., & Sonnemann, G. (2012). Gravity wave mixing and effective diffusivity for minor chemical constituents in the mesosphere/lower thermosphere. *Space Sci Rev*, *168*, 333-362. doi: 10.1007/s11214-011-9857-x

Holton, J. R. (1982). The role of gravity wave induced drag and diffusion in the momentum budget of the mesosphere. *Journal of the Atmospheric Sciences*, *39*, 791-799.

Holton, J. R. (1983). The influence of gravity wave breaking on the general circulation of the middle atmosphere. *Journal of the Atmospheric Sciences*, *40*, 2497-2507.

Holton, J. R., & Schoeberl, M. R. (1988). The role of gravity wave generated advection and diffusion in transport of tracers in the mesosphere. *Journal of Geophysical Research*, *93*, 11075–11082.

Jones Jr., M., Emmert, J. T., Drob, D. P., & Siskind, D. E. (2017). Middle atmosphere dynamical sources of the semiannual oscillation in the thermosphere and ionosphere. *Geophysical Research Letters*, *44*, 12-21. doi: 10.1002/2016GL071741

Lane, T. P., & Knievel, J. C. (2005). Some effects of model resolution on simulated gravity waves generated by deep, mesoscale convection. *Journal of the Atmospheric Sciences*, *62*, 3408-3419. doi: 10.1175/JAS3513.1

Lane, T. P., & Moncrieff, M. W. (2008). Stratospheric Gravity Waves Generated by Multiscale Tropical Convection. *Journal of the Atmospheric Sciences*, *65*, 2598-2614. doi: 10.1175/2007JAS2601.1

Lindzen, R. S. (1981). Turbulence and stress owing to gravity wave and tidal breakdown. *J. Geophys. Res.*, *86*, 9707-9714.

Liu, A. Z. (2009). Estimate eddy diffusion coefficients from gravity wave vertical momentum and heat fluxes. *Geophysical Research Letters*, *36*. doi: 10.1029/2009GL037495

Liu, H.-L. (2017). Large wind shears and their implications for diffusion in regions with enhanced static stability: The mesopause and the tropopause. *Journal of Geophysical Research: Atmospheres*, *122*, 9579–9590. (2017JD026748) doi: 10.1002/2017JD026748

Liu, H.-L. (2019). Quantifying gravity wave forcing using scale invariance. *Nature Communications*, *10*, 2605. doi: 10.1038/s41467-019-10527-z

Liu, H.-L., McInerney, J. M., Santos, S., Lauritzen, P. H., Taylor, M. A., & Pedatella, N. M. (2014). Gravity waves simulated by high-resolution Whole Atmosphere Community Climate Model. *Geophysical Research Letters*, *41*, 9106–9112. (2014GL062468) doi: 10.1002/2014GL062468

Lukovich, J. V., & Shepherd, T. G. (2005). Stirring and mixing in two-dimensional divergent flow. *Journal of the Atmospheric Sciences*, *62*, 3933-3954. doi: 10.1175/JAS3580.1

Nakamura, N. (2001). A New Look at Eddy Diffusivity as a Mixing Diagnostic. *Journal of the Atmospheric Sciences*, *58*, 3685-3701. doi: 10.1175/1520-0469(2001)058⟨3685:ANLAED⟩2.0.CO;2

Nastrom, G. D., & Gage, K. S. (1985). A climatology of atmospheric wavenumber spectra of wind and temperature observed by commercial aircraft. *Journal of the Atmospheric Sciences*, *42*, 950-960. doi: 10.1175/1520-0469(1985)042⟨0950:ACOAWS⟩2.0.CO;2

Orsolini, Y. J., Limpasuvan, V., Pérot, K., Espy, P., Hibbins, R., Lossow, S., ... Murtagh, D. (2017). Modelling the descent of nitric oxide during the elevated stratopause event of january 2013. *Journal of Atmospheric and Solar-Terrestrial Physics*, *155*, 50-61. doi: http://dx.doi.org/10.1016/j.jastp.2017.01.006

Qian, L. Y., Solomon, S. C., & Kane, T. J. (2009). Seasonal variation of thermospheric density and composition. *Journal of Geophysical Research*, *114*. doi: 10.1029/2008JA013643

Randall, C. E., Harvey, V. L., Holt, L. A., Marsh, D. R., Kinnison, D., Funke, B., & Bernath, P. F. (2015). Simulation of energetic particle precipitation effects during the 2003?2004 arctic winter. *Journal of Geophysical Research: Space*

Physics, *120*, 5035-5048. doi: 10.1002/2015JA021196
Richter, J. H., Sassi, F., & Garcia, R. R. (2010). Toward a physically based gravity wave source parameterization in a general circulation model. *Journal of the Atmospheric Sciences*, *67*, 136-156. doi: 10.1175/2009JAS3112.1
Salinas, C. C. J. H., Chang, L. C., Liang, M.-C., Yue, J., Russell III, J., & Mlynczak, M. (2016). Impacts of saber co2-based eddy diffusion coefficients in the lower thermosphere on the ionosphere/thermosphere. *Journal of Geophysical Research: Space Physics*, *121*, 12,080-12,092. doi: 10.1002/2016JA023161
Sassi, F., & Garcia, R. R. (1997). The Role of Equatorial Waves Forced by Convection in the Tropical Semiannual Oscillation. *Journal of the Atmospheric Sciences*, *54*(15), 1925-1942. doi: 10.1175/1520-0469(1997)054⟨1925:TROEWF⟩2.0.CO;2
Schunk, R. W., & Nagy, A. F. (2009). *Ionospheres, physics, plasma physics, and chemistry (2nd ed.).* Cambridge, UK: Cambridge University Press.
Smith-Johnsen, C., Marsh, D. R., Orsolini, Y., Tyssøy, H. N., Hendrickx, K., Sandanger, M. I., . . . Stordal, F. (2018). Nitric oxide response to the april 2010 electron precipitation event: Using waccm and waccm-d with and without medium-energy electrons. *Journal of Geophysical Research: Space Physics*, *123*, 5232?5245. doi: 10.1029/2018JA025418
Swenson, G. R., Salinas, C. C. J. H., Vargas, F., Zhu, Y., Kaufmann, M., Jones Jr., M., . . . Yee, J. H. (2019). Determination of global mean eddy diffusive transport in the mesosphere and lower thermosphere from atomic oxygen and carbon dioxide climatologies. *Journal of Geophysical Research: Atmospheres*, *124*(23). doi: 10.1029/2019JD031329
Swenson, G. R., Yee, Y., Vargas, F., & Liu, A. (2018). Vertical diffusion transport of atomic oxygen in the mesopause region consistent with chemical losses and continuity: Global mean and inter-annual variability. *Journal of Atmospheric and Solar-Terrestrial Physics*, *178*, 47-57.
Vosper, S. B., Brown, A. R., & Webster, S. (2016). Orographic drag on islands in the nwp mountain grey zone. *Quarterly Journal of the Royal Meteorological Society*, *142*, 3128-3137. doi: 10.1002/qj.2894
Walterscheid, R. L. (1981). Dynamical cooling induced by dissipating internal gravity-waves. *Geophysical Research Letters*, *8*, 1235-1238.
Walterscheid, R. L., & Hocking, W. K. (1991). Stokes diffusion by atmospheric internal gravity waves. *Journal of the Atmospheric Sciences*, *48*, 2213-2230.

Figure 1.

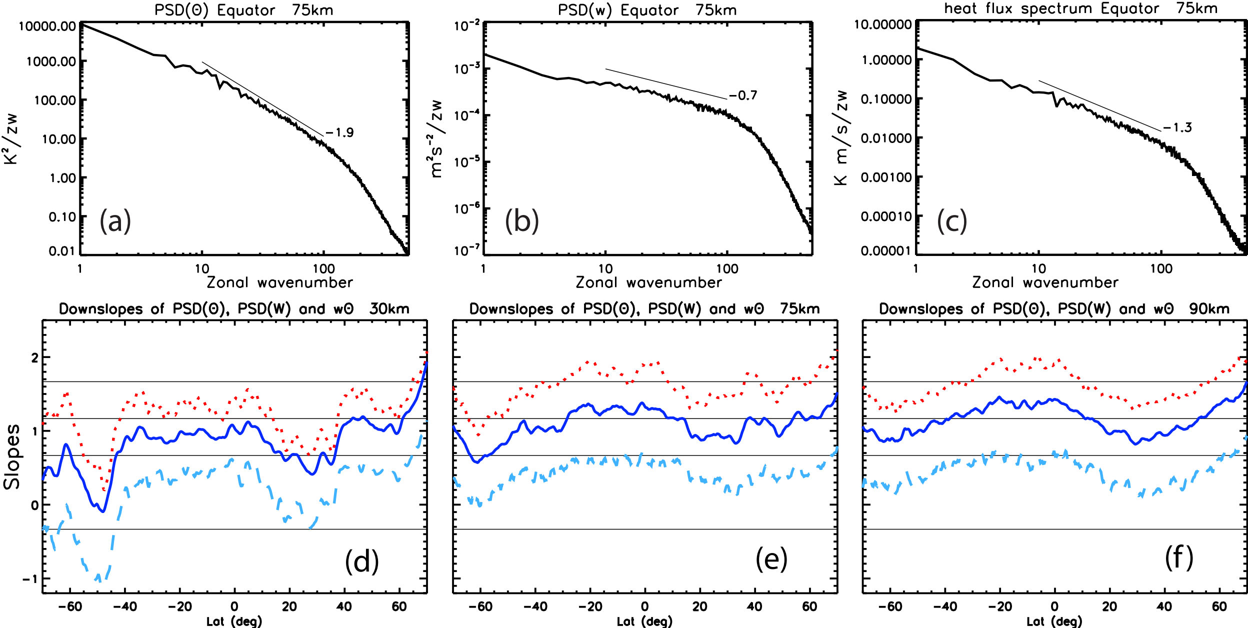

PSD(Θ) Equator 75km
K²/zw
−1.9
(a)
Zonal wavenumber
PSD(w) Equator 75km
m²s⁻²/zw
−0.7
(b)
Zonal wavenumber
heat flux spectrum Equator 75km
K m/s/zw
−1.3
(c)
Zonal wavenumber
Downslopes of PSD(Θ), PSD(W) and wΘ 30km
Slopes
(d)
Lat (deg)
Downslopes of PSD(Θ), PSD(W) and wΘ 75km
(e)
Lat (deg)
Downslopes of PSD(Θ), PSD(W) and wΘ 90km
(f)
Lat (deg)

Figure 2.

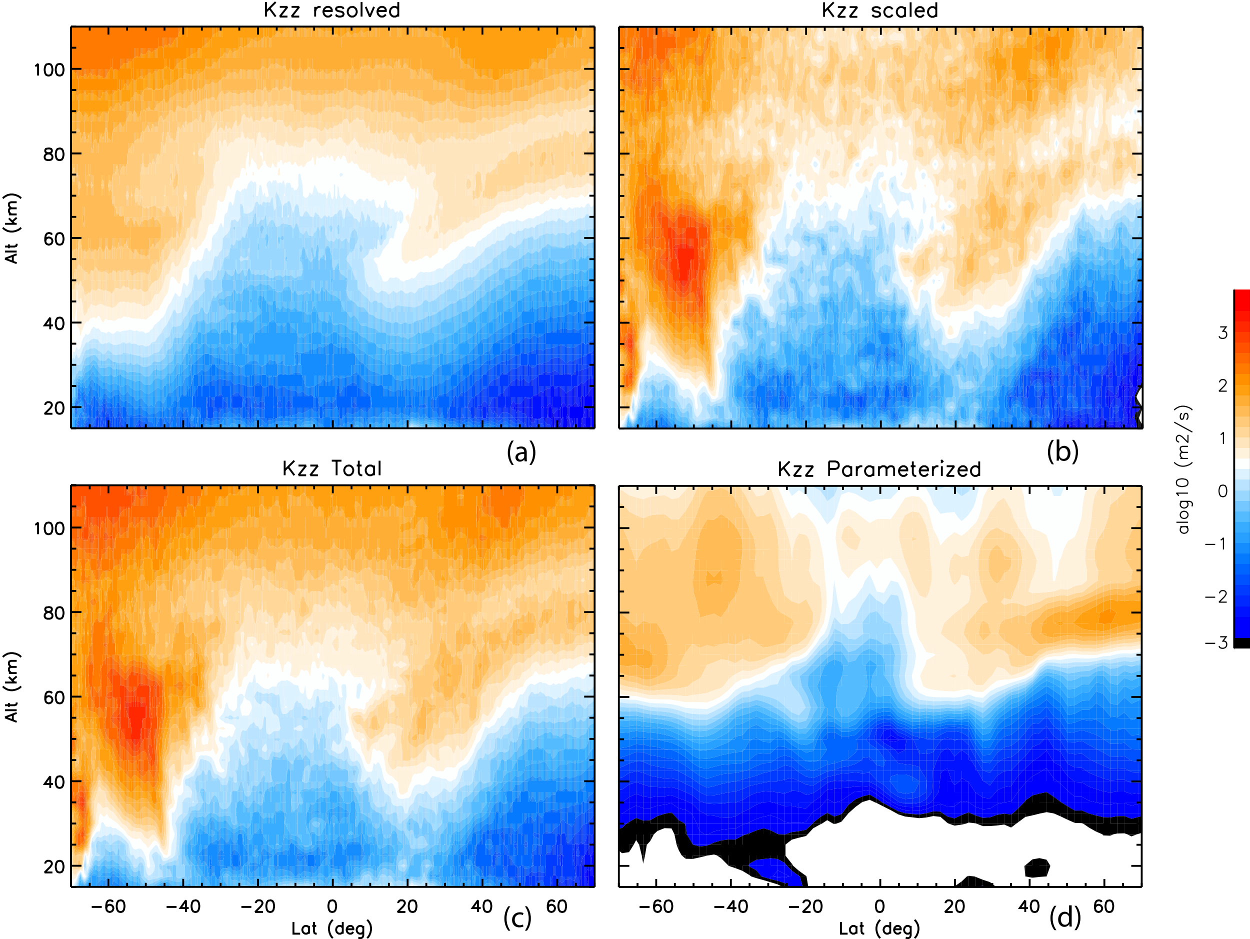

Kzz resolved
Kzz scaled
Kzz Total
Kzz Parameterized
Alt (km)
Lat (deg)
(a)
(b)
(c)
(d)
alog10 (m2/s)
100
80
60
40
20
−60
−40
−20
0
20
40
60
3
2
1
0
−1
−2
−3

Figure 3.

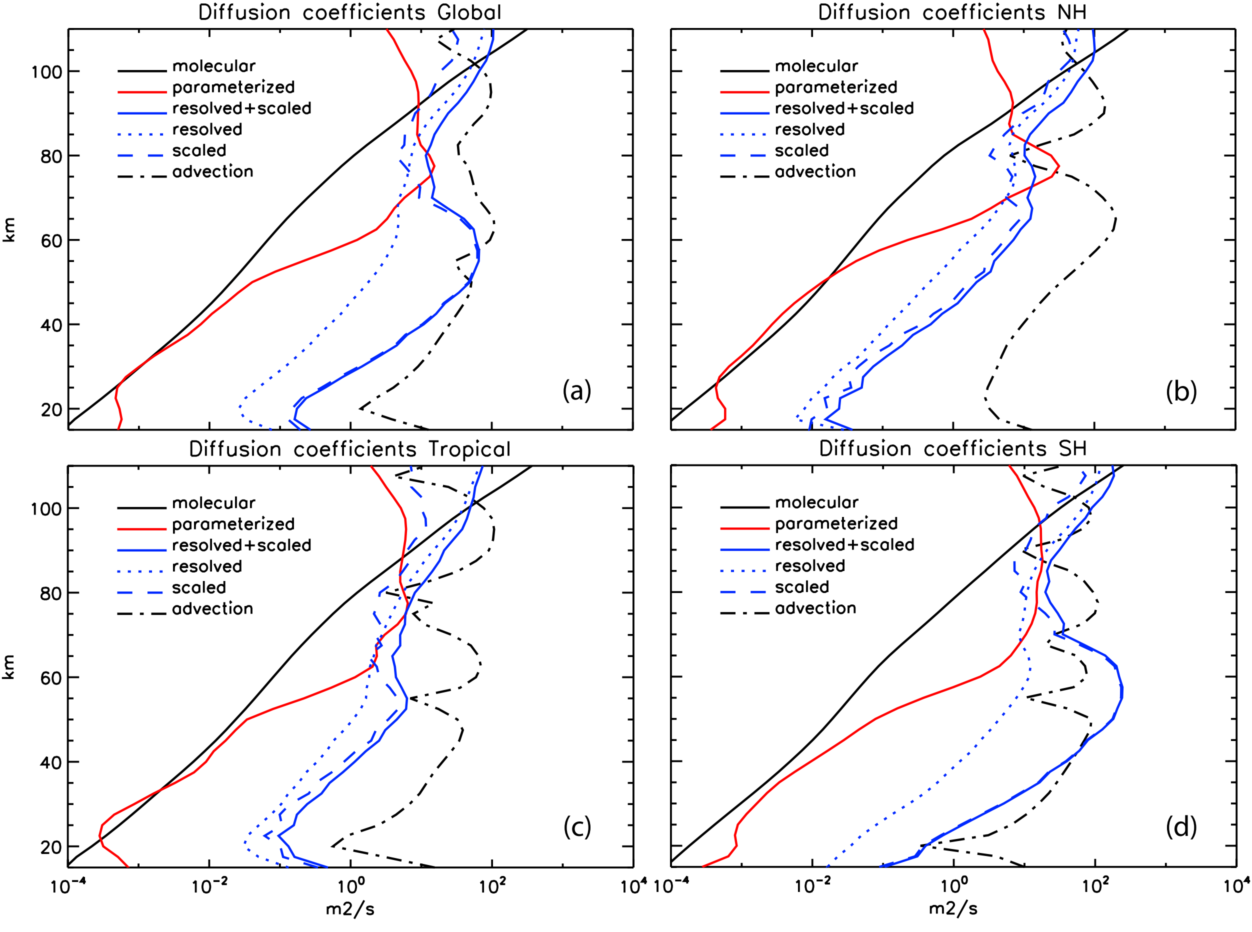

Diffusion coefficients Global
Diffusion coefficients NH
Diffusion coefficients Tropical
Diffusion coefficients SH
molecular
parameterized
resolved+scaled
resolved
scaled
advection
(a)
(b)
(c)
(d)
km
m2/s
10^{-4}
10^{-2}
10^{0}
10^{2}
10^{4}
20
40
60
80
100

Figure 4.

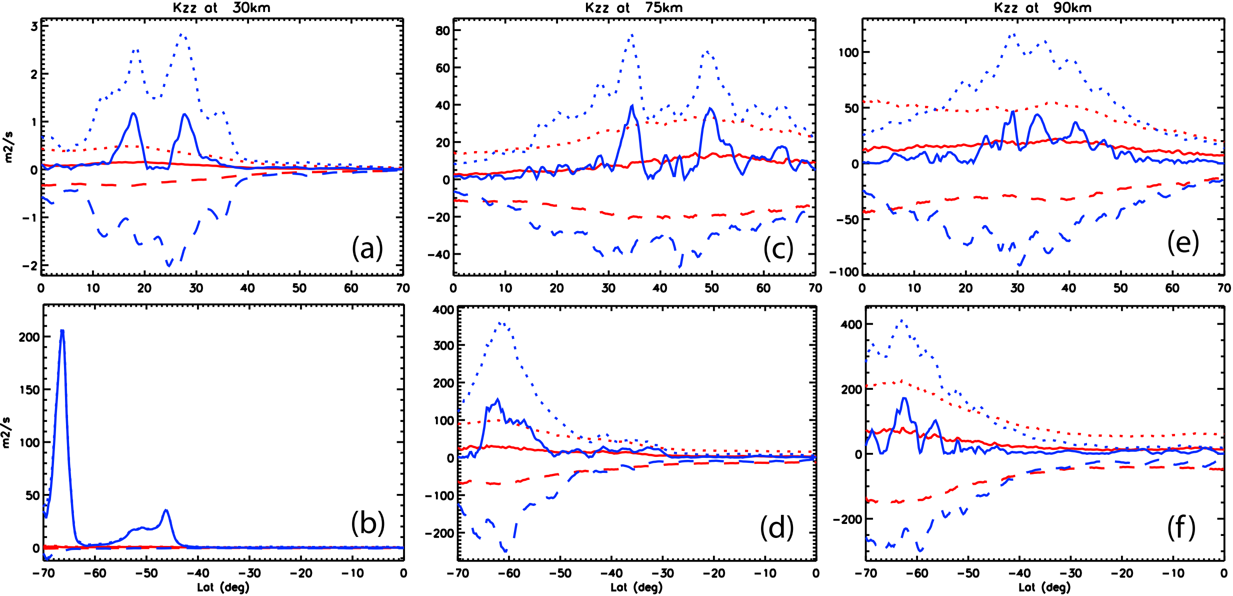
Kzz at 30km
Kzz at 75km
Kzz at 90km
m2/s
m2/s
(a)
(b)
(c)
(d)
(e)
(f)
Lat (deg)
Lat (deg)
Lat (deg)